

Merging and separation of polarization singularities in complex lattices

Mengyao Wang(王梦瑶), Tian Shi(石天), Luhui Ning(宁鲁慧), Peng Liu(刘鹏), Liangsheng Li(李粮生), and Ning Zheng(郑宁)

Citation: Chin. Phys. B, 2025, 34 (**3**): 037303. DOI: 10.1088/1674-1056/ada9da
Journal homepage: http://cpb.iphy.ac.cn; http://iopscience.iop.org/cpb

What follows is a list of articles you may be interested in

Phase changings in the surface layers of T_d-WTe_2 driven by alkali-metal deposition

Yu Zhu(朱玉), Zheng-Guo Wang(王政国), Yu-Jing Ren(任宇靖), Peng-Hao Yuan(袁鹏浩), Jing-Zhi Chen(陈景芝), Yi Ou(欧仪), Li-Li Meng(孟丽丽), and Yan Zhang(张焱)

Chin. Phys. B, 2025, 34 (**1**): 017302. DOI: 10.1088/1674-1056/ad9e9e

Quantum confinement of carriers in the type-I quantum wells structure

Xinxin Li(李欣欣), Zhen Deng(邓震), Yang Jiang(江洋), Chunhua Du(杜春花), Haiqiang Jia(贾海强), Wenxin Wang(王文新), and Hong Chen(陈弘)

Chin. Phys. B, 2024, 33 (**9**): 097301. DOI: 10.1088/1674-1056/ad5d99

Topological superconductors with spin-triplet pairings and Majorana Fermi arcs

Shi Huang(黄石) and Xi Luo(罗熙)

Chin. Phys. B, 2024, 33 (**8**): 087301. DOI: 10.1088/1674-1056/ad462f

Gate-field control of valley polarization in valleytronics

Ting-Ting Zhang(张婷婷), Yilin Han(韩依琳), Run-Wu Zhang(张闰午), and Zhi-Ming Yu(余智明)

Chin. Phys. B, 2024, 33 (**6**): 067303. DOI: 10.1088/1674-1056/ad401a

Topological charge pump by surface acoustic waves

Yi Zheng(郑一), Shi-Ping Feng(冯世平), Shi-Jie Yang(杨师杰)

Chin. Phys. B, 2016, 25 (**6**): 067301. DOI: 10.1088/1674-1056/25/6/067301

Merging and separation of polarization singularities in complex lattices

Mengyao Wang(王梦瑶)[1,2], Tian Shi(石天)[3], Luhui Ning(宁鲁慧)[4,5], Peng Liu(刘鹏)[1,†], Liangsheng Li(李粮生)[2,‡], and Ning Zheng(郑宁)[1,§]

[1] *School of Physics, Beijing Institute of Technology, Beijing* 100081, *China*
[2] *National Key Laboratory of Scattering and Radiation, Beijing* 100854, *China*
[3] *Army Engineering University of PLA Shijiazhuang Campus, Shijiazhuang* 050003, *China*
[4] *Beijing Key Laboratory of Optical Detection Technology for Oil and Gas, College of Science, China University of Petroleum-Beijing, Beijing* 102249, *China*
[5] *Basic Research Center for Energy Interdisciplinary, College of Science, China University of Petroleum-Beijing, Beijing* 102249, *China*

(Received 1 November 2024; revised manuscript received 23 December 2024; accepted manuscript online 14 January 2025)

The evolution in momentum space of bound states in the continuum (BICs) and circularly polarized states (CPSs) — as far-field polarization singularities — can be observed by controlling the geometric parameters of photonic crystals. This offers significant potential in optics and photonics. Here, we reveal that in complex lattices far-field polarization singularities can be flexibly manipulated while preserving structural symmetry. A change in topological charge for the at-Γ BIC can generate new BICs or CPSs. At an off-Γ point, a BIC can spawn from the collision of two CPSs. As the thickness of the structure increases, this BIC will meet the at-Γ BIC. The merging of BICs can induce topological charge transition and yield a large wavevector space around the Γ point with ultra-high quality (Q) factors. Our findings provide a novel degree of freedom for manipulating polarization singularities, which holds great promise in radiation modulation and singular optics.

Keywords: bound states in the continuum, circularly polarized states, topological charge, far-field polarization, photonic crystals

PACS: 73.20.At, 78.67.Pt

DOI: 10.1088/1674-1056/ada9da **CSTR:** 32038.14.CPB.ada9da

1. Introduction

The topological charges supported in photonic crystals generally arise from the singularities of far-field polarization in momentum space, which is essential for vortex beam generation and topological photonics. Polarization singularities encompass V-points (vortex singularities centered at bound states in the continuum (BICs)),[1] C-points (circularly polarized states (CPSs))[2,3] and band degeneracy points (stemming from uncertainty in the polarization direction due to band degeneracy).[4] In photonics, BICs offer an unconventional capability to ideally trap light, even though their frequencies reside within the continuous spectrum of radiative states.[5] Photonic BICs[6–9] theoretically possess infinitely high quality (Q) factors and generally exhibit topological charges with integers,[10] greatly enhancing light–matter interactions.[11,12] Consequently, they lead to various physical phenomena and applications, including strong coupling,[13] lasing,[14–16] imaging,[17] biosensing[18,19] and vortex beams.[20] By tuning appropriate structural parameters, a photonic BIC at an arbitrary k point in momentum space can be obtained.[21,22] The merging of multiple BICs can also be achieved in this way, which can improve the Q factors of Bloch modes near BICs over a wide wavevector range.[23–28] This can enhance the robustness of BICs against fabrication imperfection and is important in boosting nonlinearity[29] and quantum effects. Far-field polarization near BICs is guaranteed by structural symmetries (mirror (σ_z) symmetry, in-plane inversion ($\mathcal{I}$) symmetry and time reversal (T) symmetry),[10,30,31] often manifesting as linearly polarized vortices. Importantly, the topological properties of BICs remain robust even when structural parameters vary. When the σ_z symmetry or $\mathcal{I}$ symmetry of the photonic crystal is broken, the at-Γ BIC will split into a pair of CPSs with opposite handedness and identical topological charge.[2,32] The topological charge is a half-integer. These CPSs are only coupled with circularly polarized free-space radiation with the same handedness, which can induce strong chiral optical effects and play an important role in enhancing circular dichroism and chiral sensing. Most studies have manipulated the CPSs by breaking the structural symmetry. In this case, some new configurations of polarization singularities, such as one structural parameter simultaneously

†Corresponding author. E-mail: liupeng@bit.edu.cn
‡Corresponding author. E-mail: liliangshengbititp@163.com
§Corresponding author. E-mail: ningzheng@bit.edu.cn

© 2025 Chinese Physical Society and IOP Publishing Ltd. All rights, including for text and data mining, AI training, and similar technologies, are reserved.

supporting both BIC and CPS, are not easy to observe in the structure without σ_z symmetry or $\mathcal{I}$ symmetry.

Previous work demonstrated that CPSs can be generated from charge reversal of the at-Γ BIC in a hybrid photonic structure.[33] The infinite Q factor of the BIC enables the CPS nearby to exhibit an ultra-high Q factor, which is crucial for enhancing light–chiral matter interaction. However, the complexity of this structure with a multilayer substrate increases the difficulty of processing and manufacturing. In addition, theoretical studies have confirmed that in 2D monolayer complex lattices with σ_z and $\mathcal{I}$ symmetries, stable far-field elliptical polarization or even circular polarization near the at-Γ BIC can be achieved.[34] Nevertheless, the topological interaction between the circular polarization and BICs in this photonic crystal lacks in-depth analysis. Therefore, a topological study of polarization singularities in complex lattices is necessary. Exploring the regulation effects of structural parameters on far-field polarization may provide us with a novel degree of freedom to manipulate the polarization singularities, which is potentially applicable in singular and chiral optics. Compared with the states with high Q values near the BIC in hybrid multilayer photonic systems, monolayer complex lattices may be easier to experimentally realize these physical properties.

In this paper, we observe the dynamic evolution of far-field polarization singularities in complex lattices. It should be noted that there exists a symmetry-protected BIC at the Γ point. This at-Γ BIC is robust when the thickness of the structure is continuously tuned, and it possesses an integer topological charge. Intriguingly, the topological charge of the at-Γ BIC undergoes a transformation in the process, which can become a switch for manipulating the generation of CPSs or new BICs. Moreover, two CPSs at non-Γ points collide on a high-symmetry line, giving rise to a BIC. As parameters vary, this BIC merges with the at-Γ BIC, resulting in an increase of nearly four orders of magnitude for the Q factor in the vicinity of the merging BICs compared with the separated BIC. It is worth noting that the total topological charges are $+1$ throughout the whole process.

2. Evolution of polarization singularities near the Γ point

The complex lattice shown in Fig. 1(a) is comprised of two Si atoms ($n = 3.5$) with different radii embedded in air. $2a$ and a are constants in the x and y directions, respectively. The radii of the two Si atoms are $r_1 = 0.336a$ and $r_2 = 0.42a$, respectively. The distance separating these two atoms is a, and h represents the thickness along the z direction. Figure 1(b) shows the band structure of the complex lattice with $h = 1.52a$. The Bloch modes that we are interested in are located on the TE_1 band. Next, we quantitatively compute the dynamic distributions of topological charges in the vicinity of the Γ point as the thickness of the structure varies (see Fig. 1(c)). In momentum space, the topological charge q, carried by the far-field polarization singularity, is formally defined as follows:[30]

$$q = \frac{1}{2\pi}\oint_c \mathrm{d}\boldsymbol{k}_{||}\cdot\nabla_{\boldsymbol{k}_{||}}\phi(\boldsymbol{k}_{||}). \tag{1}$$

Here, c is an arbitrary closed path surrounding the polarization singularity in momentum space, $\boldsymbol{k}_{||}$ represents the x–y plane wave vector and $\phi(\boldsymbol{k}_{||}) = \frac{1}{2}\arg[S_1(\boldsymbol{k}_{||}) + \mathrm{i}S_2(\boldsymbol{k}_{||})]$ denotes the angle between the long axis of the corresponding polarization ellipse and the x axis. S_1 and S_2 are Stokes parameters. As shown in Fig. 1(c), when the thickness is $h = 1.13a$, there exists a symmetry-protected BIC at the Γ point, and its topological charge is -1. It should be noted that this at-Γ BIC is not induced by the folded Brillouin zone (BZ). As h gradually rises to $1.20a$, the topological charge of the at-Γ BIC undergoes a transition. Conforming to the law of topological charge conservation, two additional BICs are induced near the Γ point. Both these BICs carry a topological charge of -1 and are situated along the $+k_y$ and $-k_y$ axes, respectively. As h continues to increase, they gradually move away from the Γ point. When $h = 1.34a$, the topological charge of the at-Γ BIC reverses once again. Simultaneously, two pairs of CPSs with opposing handedness are generated in close proximity to the Γ point, and these CPSs present topological charges of $+1/2$. With further increase in thickness, the four CPSs deviate from the Γ point. When h increases to $1.50a$, the two BICs located on the k_x axis converge towards Γ point and merge with the at-Γ BIC. It can be clearly observed that the merging of BICs causes the topological charge at the Γ point to reverse again, when the thickness $h = 1.52a$. As a result, it can be observed that the at-Γ BIC with protected symmetry is robust to changes in the structural parameter h. Notably, in the whole process, topological charge conservation is satisfied. The initial transition of the topological charge at the Γ point resulted in the generation of new BICs on the high-symmetry line in the k_y direction. The second change in topological charge induced the appearance of CPSs. Lastly, it is noted that reversal of the at-Γ topological charge also occurs after the merging of multiple BICs. Furthermore, Fig. 1(d) presents the Q factor distributions close to the at-Γ BIC in momentum space for three distinct thicknesses of the structure: (i) $h = 1.50a$, (ii) $1.34a$ and (iii) $1.20a$. It becomes evident that, in comparison with the Q values simulated in the vicinity of a separated BIC in (ii) or (iii), the merging BICs in (i) significantly enhance the Q values within their neighboring regions. The detailed far-field polarization distributions corresponding to the schematic view of charge evolutions in Fig. 1(c) are shown in Appendix A.

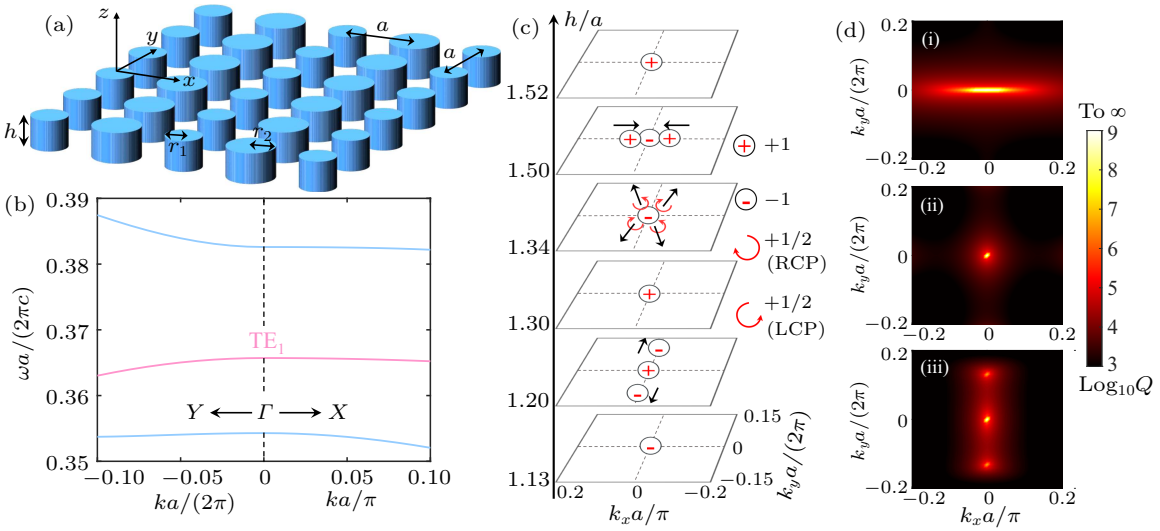


Fig. 1. (a) Schematic view of the complex lattice. (b) The band distributions of a structure with the dimensionless thickness h/a = 1.52. (c) Dynamic evolution of topological charges near the Γ point. R(L)CP is right (left)-handed circular polarization. The black arrow indicates the direction of evolution for the polarization singularity. (d) Distribution of the Q factor in momentum space: (i)–(iii) correspond to $h = 1.50a$, $1.34a$ and $1.20a$, respectively.

3. Resonance response of BIC at the Γ point

In order to further understand the properties of the at-Γ BIC, we study its resonance response. Figure 2(a) shows the band structure (TE-like) of the Bloch modes of the complex lattice that we are interested in, with $h = 1.30a$. It can be seen that the Q value is divergent at the Γ point for the band in Fig. 2(b). This indicates that there exists an at-Γ BIC for this band. Next, we simulate the transmission spectra as a function of incident wave vector k_x ($k_y = 0$) when the complex lattice is illuminated by linearly polarized light, as shown in Fig. 2(c). The detailed transmission curves T for incident wave vectors of $k_x/k_0 = 0$, 0.004, 0.006, 0.01, 0.02, 0.03 and 0.04 are displayed in Fig. 2(d). It should be noted that Fano resonance can be observed when $k_x \neq 0$. As k_x/k_0 increases from 0.004 to 0.04, the resonance linewidth γ gradually grows. The resonance disappears for $k_x = 0$. This further confirms that the Γ point is a BIC. We also fit Q values using the relationship between γ and Q ($Q = \omega_0/2\gamma$), and the fitting curve (black crosses) is shown in Fig. 2(b). It can be seen that the eigen-Q values are consistent with the fitted Q values.

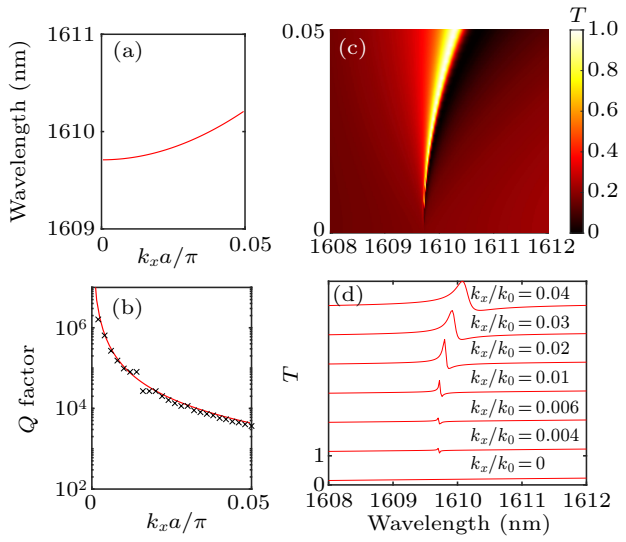


Fig. 2. (a) The band structure and (b) the Q factor (solid line) distributions of the Bloch modes in the x direction when the thickness is $h = 1.30a$. The crosses are the fitting curve from the resonance linewidth. (c) The transmission spectra with respect to incident wavelength and wave vector k_x ($k_y = 0$). (d) The relationships between the transmission spectra and k_x under linearly polarized light illumination. k_0 is π/a.

4. Characteristics of merging BICs

Next, we observe the polarization singularities map around the Γ point for $h = 1.14a$ and for $h = 1.50a$. It should be noted that there are merging behaviors of multiple BICs for both thicknesses. Figure 3 maps the distributions of far-field polarization and Stokes parameter S_3 around the merging BICs. Here, $S_3 = 2\mathrm{Im}[c_x^*(\boldsymbol{k}_{\|})c_y(\boldsymbol{k}_{\|})]$. c_x and c_y are the x and y components of the far-field polarization vector, respectively. For $h = 1.14a$, the polarization distribution is shown in Fig. 3(a). It can be seen that the nodal lines of c_x and c_y are along the k_y and k_x axes, respectively, and they intersect at the Γ point. This suggests that there indeed exists an at-Γ BIC. It can be observed that there is clear elliptical polarization near the BICs. The maximum value of $|S_3|$ is 0.9987. For Bloch modes situated on the X and Y symmetry lines, Fig. 3(c) demonstrates the correlation between the Q factors and $|\boldsymbol{k}_{||}|$. The Q values close to the BICs in the y direction satisfy $Q \propto |\boldsymbol{k}_{||}|^{-6}$ for $h = 1.14a$, while the expression of the fitting curve for the Q values is $Q \propto |\boldsymbol{k}_{||}|^{-2}$ in the x direction. It should be noted that the Q values near the at-Γ BIC in the k_y axis are almost three orders of magnitude higher than those in the k_x axis. When $h = 1.50a$, the merging BICs along the x direction are shown in Fig. 3(b). The simulations of Q values

in the x and y directions are presented in Fig. 3(d). Analysis of the fitting curves reveals that Q values near the at-Γ BIC in Fig. 3(b) scale proportionally with $|\boldsymbol{k}_{||}|^{-2}$ along the k_y axis, while those close to the merging BICs in the k_x axis adhere to the formula $Q \propto |\boldsymbol{k}_{||}|^{-6}$. As a result, the Q factors near the merging BICs (Γ–X) exceed that near the BIC (Γ–Y) by roughly five orders of magnitude. These closely distributed merging BICs allow a large wavevector space around the Γ point with high Q factors, leading to a lower decay rate (from $|\boldsymbol{k}_{||}|^{-2}$ to $|\boldsymbol{k}_{||}|^{-6}$).

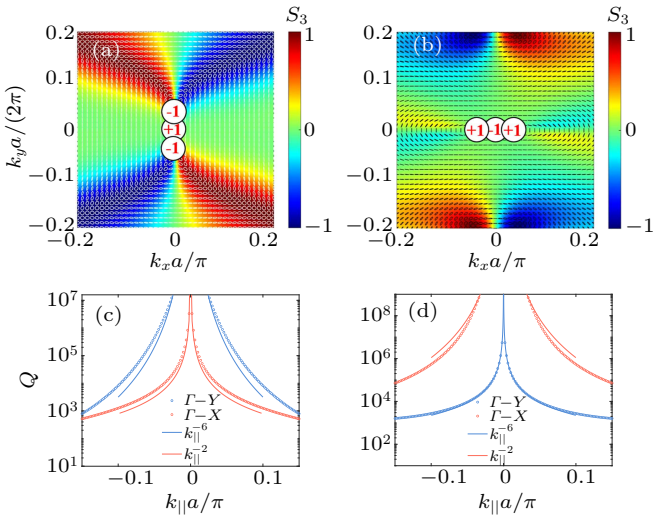


Fig. 3. The far-field polarization and Stokes parameter S_3 distributions for (a) $h = 1.14a$ and (b) $h = 1.50a$. (c), (d) Simulated Q factors (circles) and the corresponding fitting curves (solid lines) near the at-Γ BIC in the Γ–X and Γ–Y directions.

5. Merging of CPSs at the off-Γ point

Finally, we compute the origins of merging BICs on the k_y axis or k_x axis. Both BICs on the k_y axis in Fig. 3(a) are split from the charge jump of the at-Γ BIC (for details see Fig. A4 in Appendix A). Figure 4 shows the origin of the BIC on the $+k_x$ axis in Fig. 3(b). When h changes, the two half-integer charges at non-Γ points keep moving in momentum space, following the trajectories shown in Fig. 4(a). These two half-integer charges are carried by left-CPS and right-CPS, respectively. They are symmetric with respect to the k_x axis. As h increases from $1.30a$ to $1.36a$, both CPSs move closer to the k_x axis. For $h = 1.40a$, the trajectories of the two CPSs meet on the k_x axis, forming a BIC with an integer charge. When the thickness further increases, the BIC will merge with the at-Γ BIC [see Fig. 3(b)]. Similarly, the BIC on the $-k_x$ axis in Fig. 3(b) also stems from the crossing of two CPSs (see Fig. A5 in Appendix A). In momentum space, the distributions of Q factors are shown in Fig. 4(b). It is clearly observed that when the two CPSs collide on the k_x axis, a BIC with infinite Q value is generated. Due to topological charge conservation, the charge of this BIC is the sum of the charges of the two CPSs.

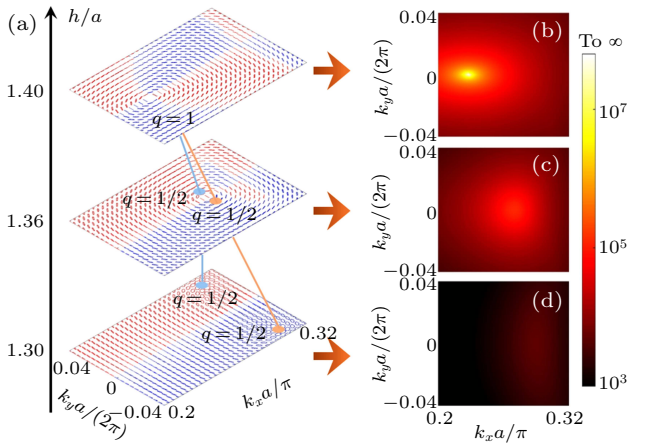


Fig. 4. (a) Trajectories traced by the two half charges (yellow and blue) at non-Γ points in momentum space as h is varied. The position $+1$ represents a BIC. The blue and yellow dots are the right-CPS (RCPS) and left-CPS (LCPS), respectively. In the polarization maps, the blue (red) represents left (right) handedness. (b) Maps of Q factors for $h/a = 1.40$, 1.36 and 1.30.

6. Conclusion

In conclusion, our findings demonstrate the diverse transformations and interactions of the far-field polarization singularities (both the BICs and CPSs) in a complex lattice without breaking $\mathcal{I}$ and σ_z symmetries. As the thickness of the complex lattice increases, the topological charge of the at-Γ BIC undergoes multiple transitions. Due to topological charge conservation, we observe the phenomenon that the at-Γ BIC can coexist with four CPSs. When the thickness is far from the coexistence region, there are BICs located on the high-symmetry line, which are generated from the collision of CPSs with the same charge. As the thickness increases, these BICs can move along the high-symmetry line. Furthermore, they merge with the at-Γ BIC to form merging BICs with extremely high Q factors in a large wavevector area. Importantly, one can experimentally obtain merging BICs and ultra-high Q circular polarization; these have significant applications in enhancing light–matter interaction, chiral responses and improving the performance of optical devices.

Appendix A

A1. Numerical methods and setups

In our study the computational cell is one unit of the complex lattice. We imposed Bloch periodic boundary conditions in the x and y directions to determine the in-plane wave vectors $\boldsymbol{k}_{||} = (k_x, k_y)$. Due to the mirror symmetry of the structure along the z axis, we only calculated the upper half of the structure. We applied perfect magnetic conductor (PMC) boundary conditions at the bottom to extract the TE-like modes of the structure. Any radiation from the lattice can be absorbed by implementing a perfectly matched layer (PML) boundary in the z direction. The band structure and intrinsic Q factor distribution of the lattice are solved using the eigenfrequency solver in COMSOL Multiphysics.

A2. Difference between at-Γ BIC in a complex lattice and a BZ folding BIC

In Fig. A1, the difference between a BIC in complex lattices and a folded BZ BIC is demonstrated. Figure A1(a) shows a schematic of the photonic crystal: (i) without the perturbation and (ii) with structural perturbation where the difference in radius between atom A and atom B is altered by the asymmetry parameter α. By introducing this structural perturbation, the periodicity of the photonic crystal in the x direction can be doubled, thereby converting the transition of non-radiative dark modes into radiative resonances. When the thickness of the structure is $1.13a$, a TE band is displayed in Fig. A1(b). The solid line represents the band without the perturbation and the blue dots depict the bands due to the periodic perturbation, with the corresponding asymmetry parameter α set to be 0.01. The blue star indicates the BIC that is currently the focus of our attention. It is evident that this BIC is not induced by the folded BZ. Furthermore, the evolution of frequency and Q factor of the at-Γ BIC with α is shown in Fig. A1(c). As α increases, the wavelength of this at-Γ BIC exhibits a blue shift. It is noted that the $\alpha = 0.2$ in the main text.

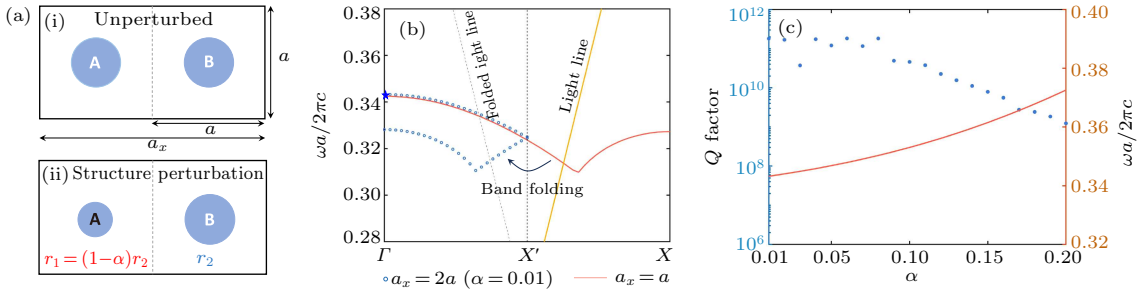


Fig. A1. (a) Schematic of the photonic crystal (i) without the perturbation and (ii) with the structure perturbation in which the difference between the radius of every two atoms is changed by the asymmetry parameter α. r_1 (r_2) is the radius of a meta-atom A (B). (b) Calculated TE band distributions of unperturbed and perturbed structures ($\alpha = 0.01$). The blue star is a BIC with structure perturbation. (c) The frequency (solid line) and Q factor (blue dot) of the at-Γ BIC vary with α. The structural thickness is $1.13a$.

A3. Analysis of far-field polarization states from structural symmetry

The far-field polarization states of our designed photonic crystal (PC) are analyzed from the perspective of structural symmetry.[10,34] As shown in Fig. A2(a), this PC is invariant under the symmetry operator $\hat{\mathcal{T}}_x\left(\frac{a_x}{2}\right)C_2^z T$. Here, C_2^z represents a 180° rotation around the z-axis through point O'. $\hat{\mathcal{T}}_x\left(\frac{a_x}{2}\right)$ is a translation of $a_x/2$ in the x direction, and T is the time inversion operator. When this symmetry operator is applied to the period part of wave function $\boldsymbol{u}_{\boldsymbol{k}_\parallel}$, it follows that $\boldsymbol{u}_{\boldsymbol{k}_\parallel}$ and $\hat{\mathcal{T}}_x C_2^z \boldsymbol{u}^*_{\boldsymbol{k}_\parallel}(\hat{\mathcal{T}}_x C_2^z \boldsymbol{r})$ have to differ at most by a phase factor

$$\begin{aligned}\boldsymbol{u}_{\boldsymbol{k}_\parallel} &= \mathrm{e}^{\mathrm{i}\theta_k}\hat{\mathcal{T}}_x C_2^z \boldsymbol{u}^*_{\boldsymbol{k}_\parallel}(\hat{\mathcal{T}}_x C_2^z \boldsymbol{r}) \\ &= \mathrm{e}^{\mathrm{i}\theta_k}\mathrm{e}^{\mathrm{i}k_x a_x/2}\left(-\boldsymbol{u}^{x,*}_{\boldsymbol{k}_\parallel}, -\boldsymbol{u}^{y,*}_{\boldsymbol{k}_\parallel}\right)\Big|_{\left(-x+\frac{a_x}{2},-y,z\right)}. \end{aligned} \tag{A1}$$

Here, θ_k is an arbitrary phase factor. By choosing $\mathrm{e}^{\mathrm{i}\theta_k} = -1$, we obtain the following expression:

$$\boldsymbol{u}_{\boldsymbol{k}_\parallel}(\boldsymbol{r}) = \mathrm{e}^{\mathrm{i}\varphi_x}\boldsymbol{u}^*_{\boldsymbol{k}_\parallel}(\boldsymbol{r}), \tag{A2}$$

where $\varphi_x = k_x a_x/2$. For $k_x \neq 0$, we get $\boldsymbol{u}_{\boldsymbol{k}_\parallel}(\boldsymbol{r}) \neq \boldsymbol{u}^*_{\boldsymbol{k}_\parallel}(\boldsymbol{r})$. The polarization vector, projected onto the x–y plane and denoted as $\boldsymbol{c}(\boldsymbol{k}_\parallel) = c_x(\boldsymbol{k}_\parallel)\hat{x} + c_y(\boldsymbol{k}_\parallel)\hat{y}$, can be complex in nature. It is found that the Stokes parameter $S_3 = 2\mathrm{Im}[c_x^*(\boldsymbol{k}_\parallel)c_y(\boldsymbol{k}_\parallel)] \neq 0$. This suggests that far-field elliptical polarization can be obtained around the at-Γ BIC in a monolayered complex lattice.

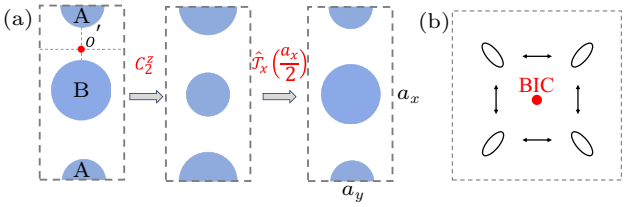


Fig. A2. (a) The complex lattice is invariant under the symmetry operator $\hat{\mathcal{T}}_x\left(\frac{a_x}{2}\right)C_2^z T$. (b) Far-field polarization states in the momentum space. The red dot denotes a BIC. The unit cell of the complex lattice includes two atoms (A and B).

A4. Temporal coupled-mode theory model

Next, the far-field polarization states of this monolayered PC are explained using the temporal coupled-mode theory (TCMT) model. When we consider a non-degenerate band, the dynamics of a resonance $A(\boldsymbol{k}_{||})$ at an in-plane wavevector $\boldsymbol{k}_{||} = (k_x, k_y)$ can be described using the TCMT[30]

$$\frac{\mathrm{d}A(\boldsymbol{k}_{||})}{\mathrm{d}t} = (\mathrm{i}\omega_0 - \gamma)A(\boldsymbol{k}_{||}) + K^{\mathrm{T}}(\boldsymbol{k}_{||})a(\boldsymbol{k}_{||}), \tag{A3}$$

$$b(\boldsymbol{k}_{||}) = Ca(\boldsymbol{k}_{||}) + D(\boldsymbol{k}_{||})A(\boldsymbol{k}_{||}), \tag{A4}$$

where $A(\boldsymbol{k}_{||})$ is the complex amplitude of the resonance, ω_0 is the resonance frequency and γ denotes the decay rate due to radiation. $a(\boldsymbol{k}_{||}) = (a_{\mathrm{s}}^{\mathrm{u}}(\boldsymbol{k}_{||}),\ a_{\mathrm{s}}^{\mathrm{d}}(\boldsymbol{k}_{||}),\ a_{\mathrm{p}}^{\mathrm{u}}(\boldsymbol{k}_{||}),\ a_{\mathrm{p}}^{\mathrm{d}}(\boldsymbol{k}_{||}))^{\mathrm{T}}$ and $b(\boldsymbol{k}_{||}) = (b_{\mathrm{s}}^{\mathrm{u}}(\boldsymbol{k}_{||}),\ b_{\mathrm{s}}^{\mathrm{d}}(\boldsymbol{k}_{||}),\ b_{\mathrm{p}}^{\mathrm{u}}(\boldsymbol{k}_{||}),\ b_{\mathrm{p}}^{\mathrm{d}}(\boldsymbol{k}_{||}))^{\mathrm{T}}$ are the amplitudes of the input and output waves, respectively. The s and p represent the types of polarization. The superscripts u and d indicate above (up) and below (down) the

structure, respectively. This is schematically illustrated in Fig. A3. Here, we assume there is no gain or absorption loss. And we consider frequencies that are below the first-order diffraction. $K(\boldsymbol{k}_{||})$ and $D(\boldsymbol{k}_{||})$ contain coupling coefficients from the resonance to the four input/output channels: $K(\boldsymbol{k}_{||}) = (K_{\rm s}^{\rm u}(\boldsymbol{k}_{||}), K_{\rm s}^{\rm d}(\boldsymbol{k}_{||}), K_{\rm p}^{\rm u}(\boldsymbol{k}_{||}), K_{\rm p}^{\rm d}(\boldsymbol{k}_{||}))^{\rm T}$, $D(\boldsymbol{k}_{||}) = (d_{\rm s}^{\rm u}(\boldsymbol{k}_{||}), d_{\rm s}^{\rm d}(\boldsymbol{k}_{||}), d_{\rm p}^{\rm u}(\boldsymbol{k}_{||}), d_{\rm p}^{\rm d}(\boldsymbol{k}_{||}))^{\rm T}$. Lastly, $C(\boldsymbol{k}_{||})$ is a direct scattering matrix and can be approximated as the response of a homogeneous slab. Since a homogeneous slab does not couple the s and p polarizations, C is a block diagonal matrix

$$C = \begin{pmatrix} C_{\rm s} & 0 \\ 0 & C_{\rm p} \end{pmatrix}, \quad C_{\rm s,p} = \begin{pmatrix} r_{\rm s,p} & t_{\rm s,p} \\ t_{\rm s,p} & r_{\rm s,p} \end{pmatrix}. \tag{A5}$$

Due to the σ_z symmetry of this PC, we only analyze the eigenmodes above the PC with thickness h_1. In this case, the input wave in the upper semispace is zero ($a_{\rm s}^{\rm u} = a_{\rm p}^{\rm u} = 0$). When the thickness is increased to $h_2 = h_1 + \Delta h$, relative to the original thickness h_1, the incident field in the lower semispace is equivalent to the reflection of the downward radiation from the thickened bottom of the modified PC

$$(a_{\rm s}^{\rm d}, a_{\rm p}^{\rm d})^{\rm T} = {\rm e}^{{\rm i}\delta}(b_{\rm s}^{\rm d}, -b_{\rm p}^{\rm d})^{\rm T}. \tag{A6}$$

Here, the additional phase $\delta = -2k_z\Delta h$ is generated by the round-trip propagation within the increased thickness Δh. Furthermore, the σ_z symmetry requires the field profile of the resonance to be either even or odd in z, so the coupling coefficients need to satisfy

$$(d_{\rm s}^{\rm u}, d_{\rm s}^{\rm d}) = d_{\rm s}(1, \sigma_z), \quad (d_{\rm p}^{\rm u}, d_{\rm p}^{\rm d}) = d_{\rm p}(1, -\sigma_z), \quad \sigma_z = \pm 1. \tag{A7}$$

When the transverse electric field (E_x, E_y) is used to determine the phases of A and a (b), we have $\sigma_z = 1$ and $\sigma_z = -1$ for TE-like and TM-like resonances, respectively. For the TE-like band under investigation, we have $\sigma_z = 1$. By substituting Eqs. (A5)–(A7) into Eq. (A4), we derive the following relationships:

$$a_{\rm s}^{\rm d} = \frac{d_{\rm s}}{{\rm e}^{-{\rm i}\delta} - r_{\rm s}} A, \quad a_{\rm p}^{\rm d} = \frac{d_{\rm p}}{{\rm e}^{-{\rm i}\delta} + r_{\rm p}} A. \tag{A8}$$

Subsequently, by substituting Eq. (A8) into Eq. (A4), and we can determine the amplitude of the upward radiation emitted by the PC

$$(b_{\rm s}^{\rm u}, b_{\rm p}^{\rm u})^{\rm T} = D'A, \quad D' = (d_{\rm s}', d_{\rm p}')^{\rm T}. \tag{A9}$$

Here,

$$d_{\rm s}' = \frac{1 + t_{\rm s}{\rm e}^{{\rm i}\delta} - r_{\rm s}{\rm e}^{{\rm i}\delta}}{1 - r_{\rm s}{\rm e}^{{\rm i}\delta}} d_{\rm s}, \quad d_{\rm p}' = \frac{1 + t_{\rm p}{\rm e}^{{\rm i}\delta} + r_{\rm p}{\rm e}^{{\rm i}\delta}}{1 + r_{\rm p}{\rm e}^{{\rm i}\delta}} d_{\rm p}.$$

The projection of the upward radiation amplitude on the x–y plane is expressed as

$$(c_x, c_y)^{\rm T} = (b_{\rm s}^{\rm u}, b_{\rm p}^{\rm u}\cos\alpha)^{\rm T}, \tag{A10}$$

where $\alpha = \arcsin(\boldsymbol{k}_{||}/\boldsymbol{k})$ is the angle between the radiation and the z axis and $\boldsymbol{k}$ is the wave vector of radiation. The Stokes parameters used to describe the far-field polarization states can be obtained by c_x and c_y

$$S_0 = |c_x(\boldsymbol{k}_{||})|^2 + |c_y(\boldsymbol{k}_{||})|^2, \tag{A11a}$$
$$S_1 = |c_x(\boldsymbol{k}_{||})|^2 - |c_y(\boldsymbol{k}_{||})|^2, \tag{A11b}$$
$$S_2 = 2{\rm Re}[c_x^*(\boldsymbol{k}_{||})c_y(\boldsymbol{k}_{||})], \tag{A11c}$$
$$S_3 = 2{\rm Im}[c_x^*(\boldsymbol{k}_{||})c_y(\boldsymbol{k}_{||})]. \tag{A11d}$$

A pure polarization state with the orientation angle ϕ and ellipticity angle χ corresponds to a set of Stokes parameters [S_0, S_1, S_2, S_3]. The following expressions demonstrate the relationship between the Stokes parameters and the longitude 2ϕ and latitude 2χ of the corresponding position located on the shell of Poincaré sphere:

$$S_0 = 1, \quad S_1 = \sin(2\phi)\cos(2\chi),$$
$$S_2 = \cos(2\phi)\cos(2\chi), \quad S_3 = \sin(2\chi). \tag{A12}$$

The ϕ and χ can be given by the Stokes parameters

$$\phi = \frac{1}{2}\arg(S_1 + {\rm i}S_2), \quad \chi = \frac{1}{2}\arcsin\left(\frac{S_3}{S_0}\right). \tag{A13}$$

According to Eq. (A9), it is found that the far-field polarization states are determined by the interference arising from variations in structural thickness. Consequently, the far-field polarization states can be manipulated by tuning the thickness of the monolayered complex lattice.

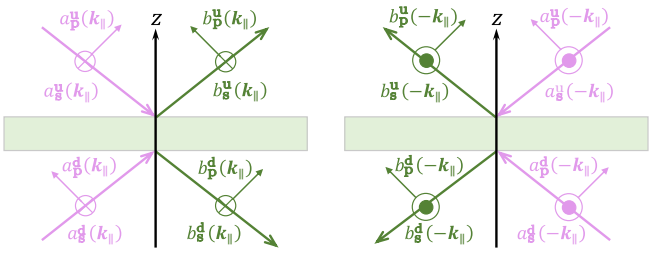


Fig. A3. Temporal coupled-mode theory model. Definition of input and output waves with $\hat{s}$ and $\hat{p}$. The direction of $\hat{s}$ is opposite for the processes at $\boldsymbol{k}_{||}$ and $-\boldsymbol{k}_{||}$, while the direction of $\hat{p}$ is same for the processes at $\boldsymbol{k}_{||}$ and $-\boldsymbol{k}_{||}$.

A5. Distributions of far-field polarization near the Γ point

The detailed far-field polarization distributions corresponding to the schematic view of charge evolutions in Fig. 1(c) are shown in Fig. A4.

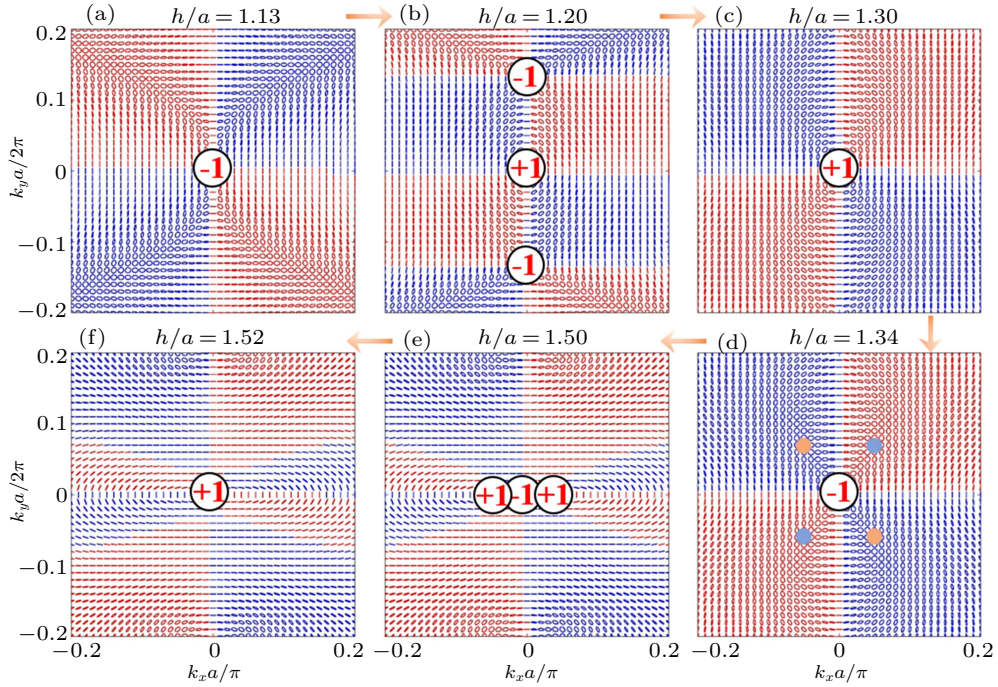


Fig. A4. (a)–(f) Detailed far-field polarization distributions corresponding to the schematic view of charge evolutions in Fig. 1(c), respectively. Blue and orange dots are the LCPSs and RCPSs, respectively.

A6. Origin of merging BICs on the $-k_x$ axis

Figure A5 shows the origin of the BIC on the $-k_x$ axis in Fig. 3(b). This process is similar to Fig. 4. The origin of the BIC on the $-k_x$ axis also stems from the crossing of two CPSs.

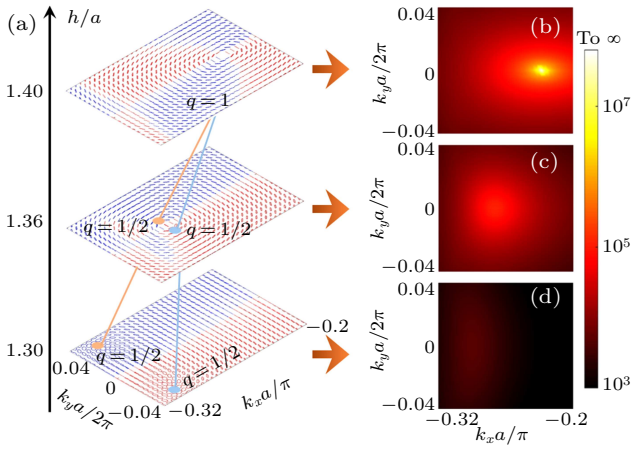


Fig. A5. (a) Trajectories traced by the two half charges (yellow and blue) at non-Γ points in momentum space as h is varied. The position of $+1$ represents a BIC. The blue and yellow dots are the RCPS and LCPS, respectively. In the polarization maps, the blue (red) represents left (right) handedness. (b) Maps of the Q factors for $h/a = 1.40$, 1.36 and 1.30, respectively.

Acknowledgement

Project supported by the National Natural Science Foundation of China (Grant No. 12374205).

References

[1] Doeleman H M, Monticone F, Hollander W D, Alù A and Koenderink A F 2018 *Nat. Photonics* **13** 397
[2] Liu W, Wang B, Zhang Y, Wang J, Zhao M, Guan F, Liu X, Shi L and Zi J 2019 *Phys. Rev. Lett.* **123** 116104
[3] Chen Y, Deng H, Sha X, Chen W, Wang R, Chen Y H, Wu D, Chu J, Kivshar Y S, Xiao S and Qiu C 2023 *Nature* **613** 474
[4] Chen A, Liu W, Zhang Y, Wang B, Liu X, Shi L, Lu L and Zi J 2019 *Phys. Rev. B* **99** 180101
[5] von Neumann J and Wigner E P 2014 *The Collected Works of Eugene Paul Wigner: Part A: The Scientific Papers* (Berlin: Springer) pp. 291–293
[6] Marinica D C, Borisov A G and Shabanov S V 2016 *Phys. Rev. Lett.* **100** 183902
[7] Wang W, Srivastava Y K, Tan T C, Wang Z and Singh R 2023 *Nat. Commun.* **14** 2811
[8] Hsu C W, Zhen B, Stone A D, Joannopoulos J D and Soljačić M 2016 *Nat. Rev. Mater.* **1** 1
[9] Liang Y, Koshelev K, Zhang F, Lin H, Lin S, Wu J, Jia B and Kivshar Y 2020 *Nano Lett.* **20** 6351
[10] Zhen B, Hsu C W, Lu L, Stone A D and Soljačić M 2014 *Phys. Rev. Lett.* **113** 257401
[11] Campione S, Liu S, Basilio L I, Warne L K, Langston W L, Luk T S, Wendt J R, Reno J L, Keeler G A, Brener I and Sinclair M B 2016 *ACS Photonics* **3** 2362
[12] Koshelev K, Lepeshov S, Liu M, Bogdanov A and Kivshar Y 2018 *Phys. Rev. Lett.* **121** 193903
[13] Wang H F, Gupta S K, Zhu X Y, Lu M H, Liu X P and Chen Y F 2018 *Phys. Rev. B* **98** 214101
[14] Song Q, Hu J, Dai S, Zheng C, Han D, Zi J, Zhang Z Q and Chan C T 2020 *Sci. Adv.* **6** eabc1160
[15] Zhong H, Yu Y, Zheng Z, Ding Z, Zhao X, Yang J, Wei Y, Chen Y and Yu S 2023 *Light Sci. Appl.* **12** 100
[16] Sun Y, Hu Z, Shi K, Guo T, Xing Y, Jin Y and He S 2023 *Adv. Opt. Mater.* **11** 2300197
[17] Conteduca D, Barth I, Pitruzzello G, Reardon C P, Martins E R and Krauss T F 2021 *Nat. Commun.* **12** 3293
[18] Romano S, Lamberti A, Masullo M, Penzo E, Cabrini S, Rendina I and Mocella V 2018 *Materials* **11** 526
[19] Wang J, Kühne J, Karamanos T, Rockstuhl C, Maier S A and Tittl A 2021 *Adv. Funct. Mater.* **31** 2104652
[20] Wang B, Liu W, Zhao M, Wang J, Zhang Y, Chen A, Guan F, Liu X, Shi L and Zi J 2020 *Nat. Photonics* **14** 623
[21] Hsu C W, Zhen B, Lee J, Chua S L, Johnson S G, Joannopoulos J D and Soljačić M 2013 *Nature* **499** 188

[22] Jiang Q, Hu P, Wang J, Han D and Zi J 2023 *Phys. Rev. Lett.* **131** 013801
[23] Jin J, Yin X, Ni L, Soljačić M, Zhen B and Peng C 2019 *Nature* **574** 501
[24] Kang M, Zhang S, Xiao M and Xu H 2021 *Phys. Rev. Lett.* **126** 117402
[25] Kang M, Mao L, Zhang S, Xiao M, Xu H and Chan C T 2022 *Light Sci. Appl.* **11** 228
[26] Bai H, Shevchenko A and Kolkowski R 2024 arXiv:2401.16105 [hep-ph]
[27] Qi X, Wu J, Wu F, Ren M, Wei Q, Wang Y, Jiang H, Li Y, Guo Z, Yang Y, Zheng W, Sun Y and Chen H 2023 *Photonics Res.* **11** 1262
[28] Lee S G, Kim S H and Lee W J 2023 *Laser Photonics Rev.* **17** 2300550
[29] Wang B, Liu J, Cui J, Liu J, Tian F, Sun W and Li L 2023 *Front. Phys.* **11** 121
[30] Yoda T and Notomi M 2020 *Phys. Rev. Lett.* **125** 053902
[31] Ovcharenko A I, Blanchard Cé, Hugonin J P and Sauvan C 2020 *Phys. Rev. B* **101** 155303
[32] Zeng Y, Hu G, Liu K, Tang Z and Qiu C W 2021 *Phys. Rev. Lett.* **127** 176101
[33] Luo H, Liu L, Xi Z, Lu Y and Wang P 2023 *Phys. Rev. A* **107** 013504
[34] Wang M, Ji C Y, Li L and Zheng N 2024 *Opt. Lett.* **49** 1401